

# In Situ Manipulation and Micromechanical Characterization of Diatom Frustule Constituents Using Focused Ion Beam Scanning Electron Microscopy

Mohammad Soleimani, Lambèrt C.A. van Breemen, Sai P. Maddala, Rick R. M. Joosten, Hanglong Wu, Ingeborg Schreur-Piet, Rolf A.T.M. van Benthem,\* and Heiner Friedrich\*

Biocomposite structures are difficult to characterize by bulk approaches due to their morphological complexity and compositional heterogeneity. Therefore, a versatile method is required to assess, for example, the mechanical properties of geometrically simple parts of biocomposites at the relevant length scales. Here, it is demonstrated how a combination of Focused Ion Beam Scanning Electron Microscopy (FIB-SEM) and micromanipulators can be used to isolate, transfer, and determine the mechanical properties of frustule constituents of diatom *Thalassiosira pseudonana* (*T.p.*). Specifically, two parts of the diatom frustule, girdle bands and valves, are separated by FIB milling and manipulated using a sharp tungsten tip without compromising their physical or chemical integrity. In situ mechanical studies on isolated girdle bands combined with Finite Element Method (FEM) simulations, enables the quantitative assessment of the Young's modulus of this biosilica;  $E = 40.0$  GPa. In addition, the mechanical strength of isolated valves could be measured by transferring and mounting them on top of premilled holes in the sample support. This approach may be extended to any hierarchical biocomposite material, regardless of its chemical composition, to isolate, transfer, and investigate the mechanical properties of selected constituents or specific regions.

including materials science and engineering, chemistry and biology.<sup>[2–5]</sup> In this respect, biocomposites such as bone, teeth, and shells are indispensable elements of living organisms and are an inspirational class of hybrid materials.<sup>[6,7]</sup> Biocomposites are formed via energy efficient and environmentally benign routes in aqueous environment at ambient temperature. They possess hierarchical ordering resulting in finely tuned properties not yet achievable by synthetic approaches.<sup>[8–10]</sup> Therefore, being able to accurately measure the properties of distinct components of biocomposites with different characteristics can inspire the fabrication of synthetic hybrids with properties tailored to specific applications.<sup>[7,11–13]</sup>

As biocomposites often possess structural and compositional heterogeneity, bulk measurements will not lead to a comprehensive determination of their underlying material properties.<sup>[14,15]</sup> A well-studied biocomposite is nacre which demonstrates outstanding mechanical properties resulting from the stacking of aragonite tiles and organic layers (resembling bricks and mortar).<sup>[16]</sup> Not only does its mechanical performance vary with respect to the various loading directions but also different failure mechanisms have been proposed under different loading conditions.<sup>[17]</sup> It has been suggested that its excellent mechanical performances, such as Young's modulus in the range of 60–70 GPa,<sup>[18]</sup> depends on several parameters at different length scales, ranging from

## 1. Introduction

Hybrid materials made from organic and inorganic compounds often possess superior combinations of physical and chemical properties compared to their individual components, which make them attractive for many technological applications.<sup>[1]</sup> The development of advanced hybrid materials involves many disciplines

including materials science and engineering, chemistry and biology.<sup>[2–5]</sup> In this respect, biocomposites such as bone, teeth, and shells are indispensable elements of living organisms and are an inspirational class of hybrid materials.<sup>[6,7]</sup> Biocomposites are formed via energy efficient and environmentally benign routes in aqueous environment at ambient temperature. They possess hierarchical ordering resulting in finely tuned properties not yet achievable by synthetic approaches.<sup>[8–10]</sup> Therefore, being able to accurately measure the properties of distinct components of biocomposites with different characteristics can inspire the fabrication of synthetic hybrids with properties tailored to specific applications.<sup>[7,11–13]</sup>

M. Soleimani, S. P. Maddala, R. R. M. Joosten, H. Wu, I. Schreur-Piet, R. A. T. M. van Benthem, H. Friedrich  
Laboratory of Physical Chemistry  
and Center for Multiscale Electron Microscopy  
Department of Chemical Engineering and Chemistry  
Eindhoven University of Technology  
Groene Loper 5, Eindhoven 5612 AE, The Netherlands  
E-mail: r.a.t.m.v.benthem@tue.nl; H.Friedrich@tue.nl

L. C. A. van Breemen  
Polymer Technology  
Materials Technology Institute  
Department of Mechanical Engineering  
Eindhoven University of Technology  
Groene Loper 15, Eindhoven 5612 AE, The Netherlands  
R. A. T. M. van Benthem  
DSM Materials Science Center, Netherlands  
P.O. Box 18, Geleen 6160 MD, The Netherlands  
H. Friedrich  
Institute for Complex Molecular Systems  
Eindhoven University of Technology  
Groene Loper 5, Eindhoven 5612 AE, The Netherlands

 The ORCID identification number(s) for the author(s) of this article can be found under <https://doi.org/10.1002/smt.202100638>.

© 2021 The Authors. Small Methods published by Wiley-VCH GmbH. This is an open access article under the terms of the Creative Commons Attribution License, which permits use, distribution and reproduction in any medium, provided the original work is properly cited.

DOI: 10.1002/smt.202100638

nano to micrometers.<sup>[14]</sup> Another, structurally complex biocomposite is the diatom frustule, i.e., the siliceous exoskeletons of unicellular photosynthetic algae, diatoms.<sup>[19]</sup> Diatoms are distributed throughout most aquatic environments, in an amazing multitude of shapes, and in sizes ranging from 2 to 2000  $\mu\text{m}$  in diameter or length.<sup>[20]</sup> The diatom frustule, composed of two valves and a number of overlapping girdle bands, possess a species-specific morphology of micro and nanopatterns.<sup>[21,22]</sup> The current understanding is that girdle bands and valves are different in terms of their structures, functions, and mechanical performance.<sup>[23–26]</sup> However, the basic mechanical properties such as Young's modulus of the frustule constituents have only been measured independently for a large diatom species.<sup>[27]</sup>

Mechanical properties of diatoms have been mainly measured by AFM on the frustule of various diatom species.<sup>[28,29]</sup> However, obtained results rather provide insights into indentation of the frustule's morphology than a quantitative measure of mechanical properties of specific parts, while an independent observation of the indentation action missing. More convincingly, in situ mechanical testing of diatoms have also been conducted in SEM, either on whole frustules<sup>[30,31]</sup> or on frustule fragments using three-point bending.<sup>[27]</sup> However, indentation on the entire frustule makes it difficult to distinguish the mechanical responses of the girdle bands from those of the valves. Also, due to the presence of complex hierarchical structures in the valves, a geometrically simplified FEM simulation is not adequate for a precise determination of basic mechanical properties such as the Young's modulus. Owing to the wide variation of diatom sizes, the mechanical property measurements of the frustule segments in SEM were hitherto limited to large diatoms such as *Coscinodiscus* sp. ( $\approx 150 \mu\text{m}$  in diameter). The sample preparation for the SEM measurements of this species required harsh chemical separation of the frustule segments using  $\text{H}_2\text{O}_2$  and  $\text{HCl}$ , which not only resulted in unintentional fracture of the segments,<sup>[27]</sup> but may also have significantly altered the compositional and mechanical properties of the biosilica.<sup>[32]</sup>

Above examples demonstrate the importance of developing new techniques to assess the basic mechanical properties of biocomposites at all relevant length scales. This requires precise isolation of different parts of the diatom frustule and measurements on these individual constituents. Electron Microscopy (EM) has been used as an imaging tool to characterize materials at the relevant micro and nanoscales in situ.<sup>[33–36]</sup> Scanning Electron Microscopy (SEM) may be combined with Focused Ion Beam (FIB)

micromachining and micromanipulators, allowing imaging and manipulation of micro and nano-objects in real time.<sup>[37]</sup> FIB-SEM micromachining is involved in the fabrication and observation of micro and nano-test specimens,<sup>[38]</sup> and by using a micromanipulator, objects can be picked up, transferred and released from a bulk sample to a particular substrate for further investigation.<sup>[39,40]</sup> Using a combination of FIB-SEM and micromanipulators, characterization of the mechanical properties of materials on various length scales becomes feasible.<sup>[41,42]</sup> In situ mechanical testing such as bending, indentation, and compression tests via micromanipulators inside SEM has been one of the attractive approaches for observing the deformation behaviors of micro and nano-scale materials.<sup>[43–45]</sup> However, to the best of our knowledge there has been no investigation that combined in situ isolation, manipulation, and mechanical characterization of individual constituents of biocomposites such as diatom frustules.

In this manuscript, we demonstrate a flexible workflow exploiting FIB-SEM with micromanipulators to isolate, prepare, and characterize selected biosilica segments of diatoms to determine their Young's modulus, on the micrometer scale. As a model and example of biocomposite materials, the diatom frustules of *Thalassiosira pseudonana* (*T.p.*), grown at different salinities, were used.<sup>[46]</sup> Using our specific sample fabrication, and in situ deformation experiments supported by FEM simulations, the Young's modulus of biosilica diatom frustule constituents, i.e., girdle bands could be quantitatively assessed. The presented methodology may be employed for other in situ characterization of the constituents of hierarchical biocomposites that cannot be accessed by other means.

## 2. Results and Discussion

An overview of the entire sample preparation and characterization workflow is shown in **Figure 1**. After deposition of the extracted intact diatom frustules on the SEM sample support, FIB micromachining is used to detach the valves from the girdle bands (Figure 1, Step 1). Subsequently either the girdle bands or the valves are transferred to specific locations for in situ deformation experiments (Figure 1, Step 2a and 2b). Mechanical tests are carried out using a force measurement sensor (FMT-120) attached to a micromanipulator in combination with information from SEM images to obtain a load-displacement curve (Figure 1, Step 3a and 3b). Finally, by Finite

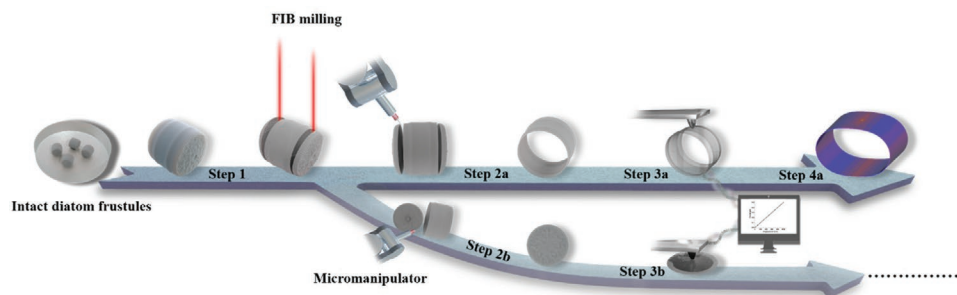


**Figure 1.** Scheme of in situ isolation, transfer, and deformation of constituents of diatom frustule. (Step 1) FIB milling on intact diatom frustule; (Step 2a and 2b) isolation and transfer of valves and girdle bands; (Step 3a and 3b) deformation tests on isolated girdle bands and valves; (Step 4) employing the experimental data for determining the Young's modulus of the girdle bands by FEM simulations.

Element Method (FEM) simulations of the load-displacement curve using all relevant morphological information the Young's modulus of the biocomposite, girdle bands, can be derived (Figure 1, Step 4).

In the following sections each step of above workflow will be described and discussed, starting with a detailed investigation of the morphological parameters of frustule of *T.p.* in dependence of the growth conditions, including mild extraction of the frustules from living cells, preserving the physical and chemical integrity of the natural biocomposite as best as possible, and deposition on the SEM sample substrate.

### 2.1. Morphological Parameters of *T.p.*

*T.p.* is one of the smallest and most well-known diatoms. It is of great interest to scientists due to its fully sequenced genome and high adaptability to various environmental conditions, including salinity levels.<sup>[47–49]</sup> In this study, salinity levels found in nature, namely 28, 36, and 46 PSU (Practical Salinity Unit),<sup>[46,50]</sup> were employed in the growth medium in order to gain insights into the effect of this factor on the mechanical and morphological parameters of *T.p.* The frustules were extracted from the living cells by washing with ethanol and subsequent drying in a critical point dryer in order to, not only reduce the impact of the extraction process on the natural chemistry and morphology, but also to prevent the collapse of the frustule (more details are provided in the Experimental Section and Figure S1, Supporting Information). The dried frustules were then deposited on SEM stubs or TEM grids for morphological analysis. *T.p.* is a centric diatom with a cylinder-shaped cell wall that contains two valves/lids connected by several overlapping girdle bands (Figure 2a). As shown in Figure 2b, the valve's exterior surface exhibits patterns of ribs known as costae connected by cross-connections, forming areole pores. Within the

areole, some small pores called cribrum are located. Unlike the exterior surface, the interior surface of the valves are relatively smooth without ribs and the cribrum pores clearly being visible (Figure 2c). Figure 2d presents a girdle band, isolated by ultrasonication, which has porous and nonporous regions. SEM-Energy-Dispersive X-ray Spectroscopy (SEM-EDS) elemental mapping of an intact frustule, from both valve and girdle bands views, shows a homogenous distribution of silicon alongside oxygen and carbon, indicating their uniform distribution throughout the entire diatom frustule (Figure 2e–h).

To establish whether morphological characteristics such as thickness, pore size, and overall size of the valves and girdle bands of *T.p.* were altered by increasing the salinity levels in the growth medium, TEM and SEM image analyses were conducted. Varying salinity levels did not change the valve diameter and the girdle bands length of the frustule (Figure S2, Supporting Information). High magnification SEM images of the interior surface of the valves grown at different salinities show that the cribrum pore size was unchanged when the salinity was increased from 28 to 36 PSU, with the cribrum pore size measuring  $20\pm 3$  and  $19\pm 4$  nm in diameter, respectively. At a salinity of 46 PSU the cribrum pore size increased to  $27\pm 3$  nm (Figures S3 and S4, Supporting Information). The thicknesses of the girdle bands and valves were measured from TEM images,<sup>[51]</sup> (Figures S5 and S6, Supporting Information). The mean thicknesses of the girdle bands for 28 and 36 PSU were  $26\pm 5$  and  $25\pm 5$  nm, respectively, whereas at 46 PSU girdle bands had a thickness of  $21\pm 4$  nm.

### 2.2. Step 1 and 2: Detaching the Valves from Girdle Bands

The first step in the procedure to determine the mechanical properties of the frustule was to isolate the valves from the girdle bands. Since the thickness of the girdle bands was less

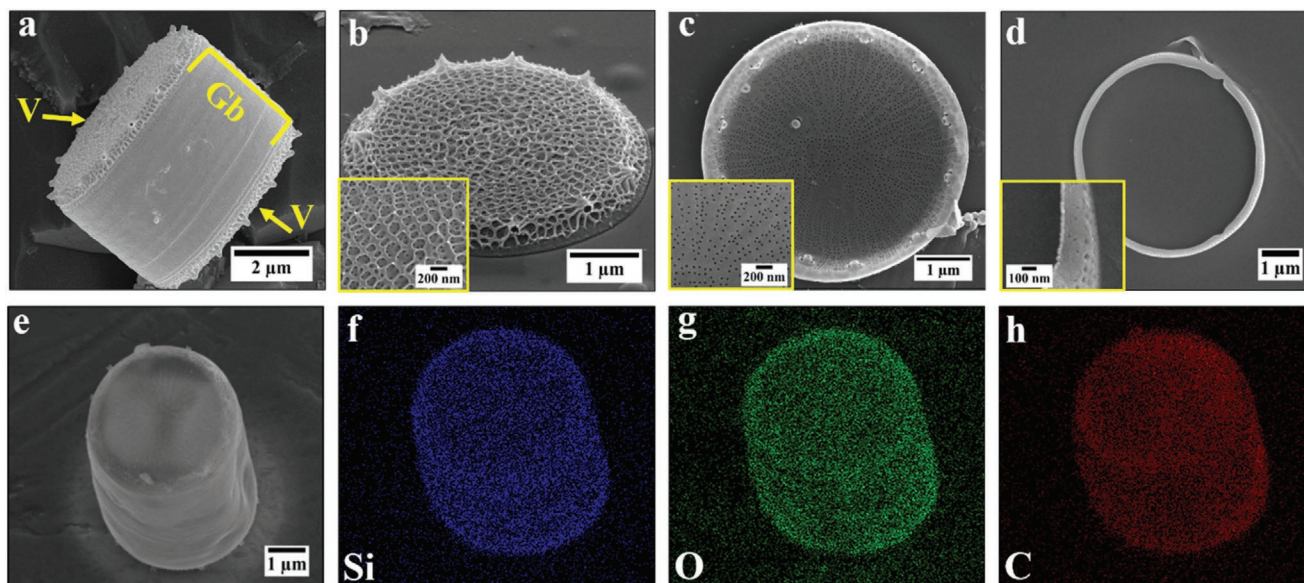


**Figure 2.** a) SEM images of intact mature frustule of *T.p.* (V and Gb referring to valve and girdle bands, respectively); b) exterior surface of an isolated valve; c) interior surface of an isolated valve; d) individual girdle band; Insets in (b), (c), and (d) show high magnification images; e–h) SEM-EDS elemental maps of an entire frustule viewed from the direction of both valve and girdle bands.

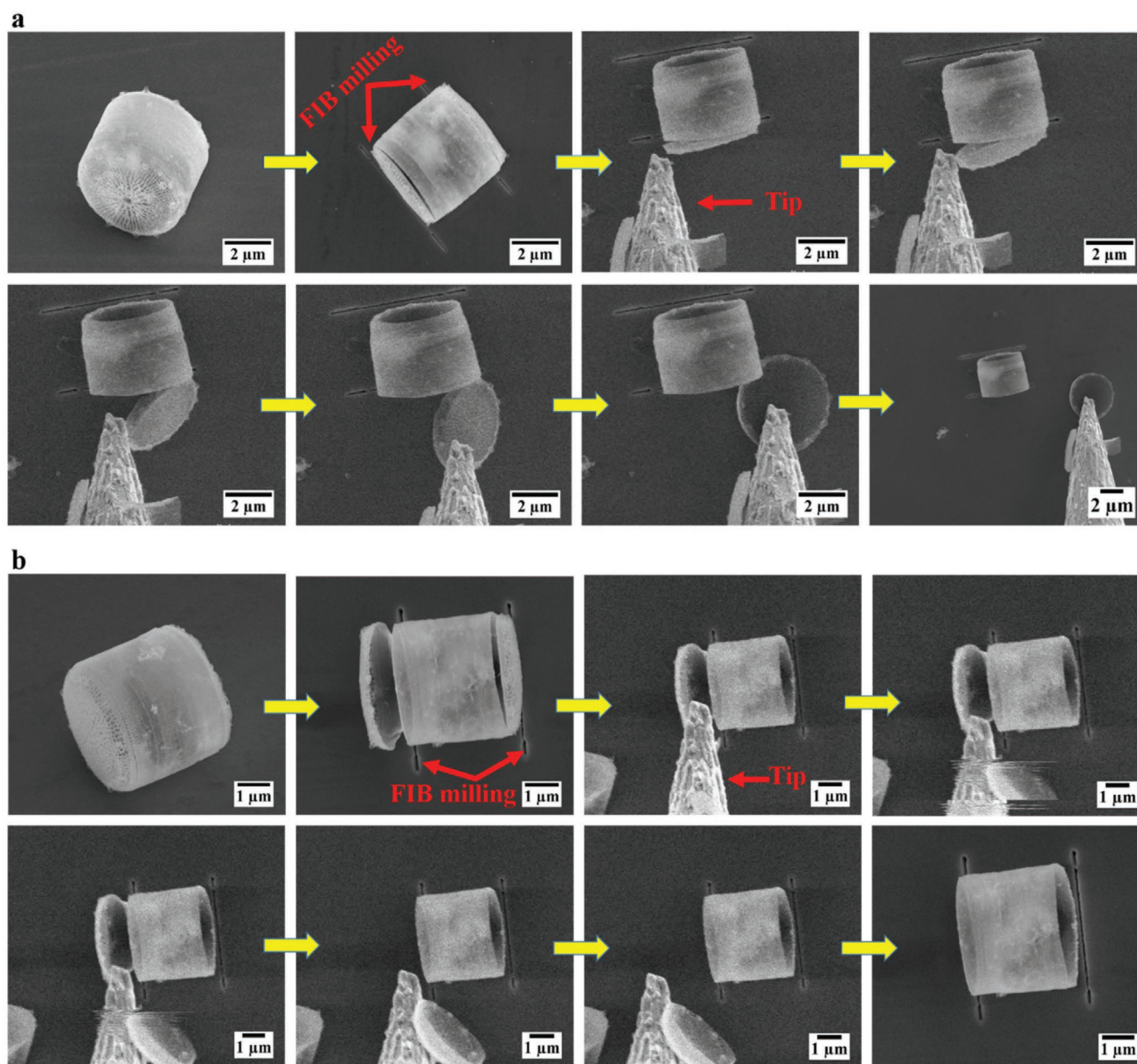


**Figure 3.** a) Mechanical manipulation: Intact frustule of *T.p.* positioning on its girdle bands, cutting the valves with FIB milling, from left to right: sequence of mechanical manipulation for removing the valve via a tungsten tip, an isolated girdle bands after complete separation of the valves was obtained; b) (from left to right) sequence of FIB milling and electrostatic manipulation of an isolated valve from the girdle bands of an intact frustule.

than 30 nm and the inside of the cell was empty, resembling a hollow cylinder, the lowest possible ion current (1.5 pA) was employed during the FIB milling procedure to prevent collapsing the structure. **Figure 3a** shows an intact frustule of *T.p.* laying on its girdle bands. By FIB milling, the valves were precisely detached from the girdle bands. Then, one of the detached valves was moved using the sharp tungsten tip to the right side of the frustule where it was ultimately separated without damaging the girdle bands. The insignificant adhesive force between the detached valve and girdle bands, which may be due to the milling process or electrostatic in nature, was overcome by slightly pushing the valve toward the girdle bands. Finally, after complete separation of the valve via the microma-

nipulator tip, the valve was removed entirely to eliminate its hindering effect during the deformation experiments on the girdle bands (see also Movie S1, Supporting Information). As shown in **Figure 3a** this manipulation was entirely performed by push-pull or mechanical manipulation,<sup>[52]</sup> with a sharp tungsten tip which did not damage the valves or girdle bands.

The second method employed to isolate the valves was based on electrostatic manipulation. The detached valves were retained on the silicon wafer by various attractive forces such as van der Waals<sup>[39]</sup> and adhesive forces induced by the ion beam during the milling process. The charging of the non-grounded tungsten tip caused by electron beam illumination led to the attraction of the specimen,<sup>[53]</sup> here the detached valves to the

tip. The charged tip was brought into contact with the detached valve. When the attractive forces between the tip and valve (likely van der Waals and electrostatic) were stronger than the aforementioned forces, which held the valve on the substrate, the valve attached to the tip. Figure 3b shows a series of images of electrostatic manipulation which finally removed the valves and a hollow cylinder-shaped structure was obtained (see also Movie S2, Supporting Information). Releasing the electrostatically attached valve from the tip was performed by touching the substrate with the valve and shifting the electron beam irradiation away from the tip. Various parameters such as the electron energy, sample size and shape, roughness of the sample, and distance between the tip and sample are important in electrostatic manipulation inside SEM.<sup>[54]</sup> It should be noted that it was difficult to selectively choose between one of the two aforementioned manipulations over the other. In general, there may be a link between the type of manipulation and some factors such as the direction between the tip and the valve, which can cause different contact areas, the gap between the detached valve and girdle bands, and contact area between the valve and substrate. Nevertheless, further research should be undertaken to investigate the exact causes which led to electrostatic and mechanical manipulation of the valves.

### 2.3. Step 3a: In Situ Deformation Tests on Isolated Girdle Bands

In order to investigate the mechanical behavior of girdle bands in situ deformation tests were performed with a force measurement sensor FMT-120 which was mounted on the micromanipulator. SEM images were continuously acquired throughout the whole process to follow the deformation behavior of the girdle bands. A series of controlled displacement experiments were conducted on the isolated girdle bands of *T.p.* which had been grown at different salinities, 28 and 46 PSU. Throughout the deformation experiments, the force measurement system (FMS) provides force-time data which could be converted to force-displacement information via image analysis of the SEM micrographs. Some images from the deformation tests on isolated girdle bands of *T.p.* grown at different salinities are presented in Figure 4a together with representative load-displacement curves. As shown in the SEM images, the

girdle bands completely returned to their original shape after retracting the tip, without a significant plastic deformation, suggesting elastic properties of these parts (see also Movie S3, Supporting Information). An equal mean maximum force ( $n = 3$ ) of  $0.50 \pm 0.02$  and  $0.52 \pm 0.03 \mu\text{N}$  were required for about 1050 nm deformation of girdle bands grown at 28 and 46 PSU, respectively. As shown in Figure 4b, the aforementioned 20% difference in thickness due to the different salinity in the growth medium surprisingly did not significantly impact the mechanical behavior of girdle bands. Here it is important to note that it is known that the frustules of *T.p.* grown at 46 PSU is more condensed than 26 PSU.<sup>[49]</sup> Hence, it could be hypothesized that despite the difference in thickness of the girdle bands at 28 and 46 PSU, the difference in the condensation state of the biosilica might cause close to identical mechanical behaviors. The experimental nonlinearities in the load-displacement curves, as well as the very limited plastic deformation between load-unload curve observed during the first cycle of the experiment (Figure S7, Supporting Information) are probably due to rearrangements between individually overlapping girdle bands (Figure S8, Supporting Information) during the deformation tests. Interestingly, no fracture/failure was detected even when the girdle bands were completely compressed and touching the opposing side. The girdle bands showed fully elastic recovery after the tip retraction. To determine whether the organic compounds within the girdle bands contributed to this behavior, the same deformation experiment was performed on a set of thermally treated (450 °C) girdle bands. In this case a noticeable irreversible deformation was observed upon deformation and tip retraction in this sample (Figure S9, Supporting Information). While this is a first indication of the role of organics in attaining elasticity of girdle bands, considerably more work will need to be done to determine the effects of various organic compounds such as long-chains polyamines, silaffins, and other macromolecules<sup>[22]</sup> within the frustules of diatoms on their mechanical performance.

### 2.4. Step 4: FEM Simulation and Deriving the Young's Modulus

Based on the experimental results for the required force causing a given displacement and also SEM and TEM image

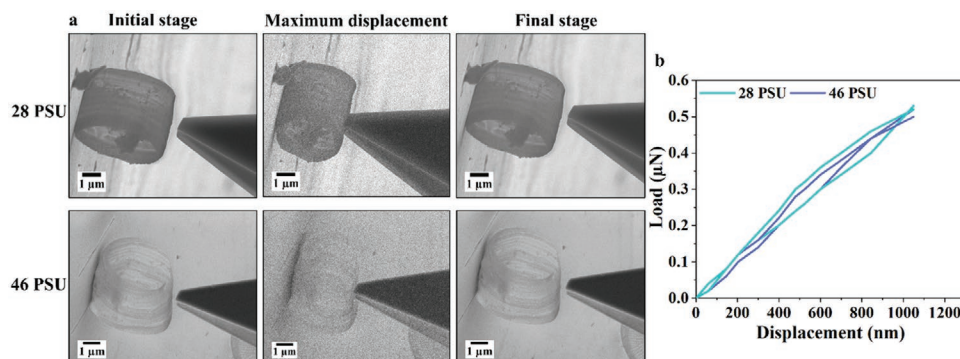


**Figure 4.** a) In situ mechanical experiments on isolated girdle bands grown at different salinity (top) 28 PSU; (bottom) 46 PSU. SEM images at different states of the experiment, before, during, and after the deformation tests (poor resolution of images at the maximum displacement is due to the shorter dwell time of imaging during the deformation tests); b) representative load-displacement curves for 28 PSU (blue) and 46 PSU (green) during the displacement-controlled deformation. For clarity only two of the obtained curves per salinity are shown.

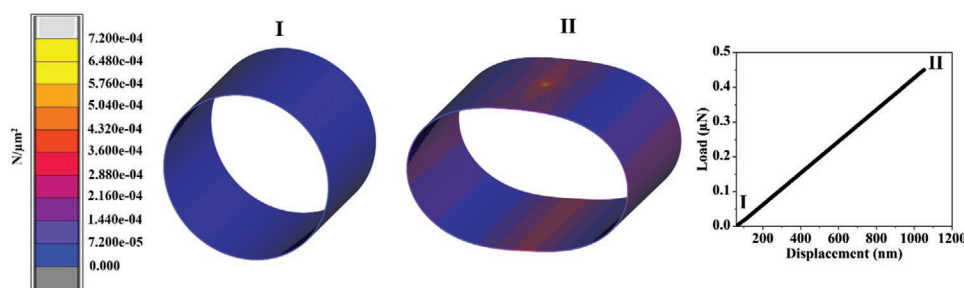


**Figure 5.** The images show the situation in the initial undeformed configuration, I, as well as the situation at maximum deformation, II, of the girdle bands as a result of the deformation with the FMT tip. For clarity, the FMT tip is omitted from the images. The colors in the images represent the equivalent Von Mises stress as indicated by the scale bar on the left. The graph on the right-hand side displays the force response in dependence of deformation.

analysis, FEM simulation was employed to determine the intrinsic mechanical properties of girdle bands (grown at 28 PSU), i.e., its Young's modulus. **Figure 5** exhibits the initial and maximum displacement states of the model and its corresponding elastic load-displacement curve. FEM simulation illustrated that for 0.45  $\mu\text{N}$  force causing 1050 nm displacement, sufficiently close to the obtained experimental value, a Young's modulus  $E$  of 40.0 GPa was determined for our biosilica. This result is comparable to the reported average Young's modulus of biosilica from *Coscinodiscus sp* (36.4 GPa) obtained by three-point bending tests on a large lamella of its frustule inside an SEM. <sup>[27]</sup>

## 2.5. Effect of Accelerating Voltage and Deformation Cycles on the Mechanical Behavior of Girdle Bands

To assess whether and to what extent the mechanical behavior of the girdle bands could be affected by the experimental conditions, in situ deformation experiments were carried out at various accelerating voltages inside the SEM chamber. As can be seen in **Figure 6a**, despite applying various accelerating voltages, from 3 kV (electron dose:  $D = 7.5 \times 10^{-7} \text{ C cm}^{-2}$ ) to 30 kV ( $D = 3.2 \times 10^{-6} \text{ C cm}^{-2}$ ), the girdle bands retained their elasticity. By increasing the accelerating voltage from 3 to 10 kV the amount of applied force for a given displacement remained constant at  $0.50 \pm 0.02 \mu\text{N}$ . However, as shown in **Figure 6b**, from 10 to 20 kV there was an enhancement in resistance to deformation ( $0.75 \mu\text{N}$  at maximum), indicating increased hardening of the girdle bands by electron irradiation. Further increasing the accelerating voltage to 30 kV resulted in an even more pronounced effect. As shown in the graph, approximately twice the force was required for the same amount of displacement in comparison to 10 kV. These results may be explained by the fact that increasing the energy of the impinging electron inside the EM before and during the mechanical testing can lead to the conversion of less condensed silica structures to more condensed silica networks. <sup>[55,56]</sup> Since the wall thicknesses of the girdle bands at different acceleration voltages are identical, the observed increase in stiffness is therefore not geometry related. This behavior can only be explained by an increase in the elastic/Young's modulus, which in turn is directly related to its density,<sup>[57]</sup> i.e., higher density gives a higher modulus.

In addition, in order to monitor effects of the number deformation cycles on the mechanical behavior of the girdle bands, a series of deformation test was conducted on one specific set of girdle bands for a given displacement. As shown in **Figure 6c**, the girdle bands kept their elastic behaviors upon deformation and tip retraction without noticeable irreversible deformation throughout various cycles. The maximum forces for a given displacement were measured for 10 consecutive cycles (**Figure 6d**). Interestingly, it can be seen from the data in the graph that the number of deformations did not influence the required force for  $\approx 1 \mu\text{m}$  displacement of the girdle bands, indicating the independence of the mechanical performance of girdle bands on the number of deformation cycles.

## 2.6. Step 2b and 3b: Transferring and In Situ Deformation on Isolate Valves

The mechanical properties of the detached valves were also investigated. To this end, holes were drilled in the substrate by FIB milling and the valves were mounted on these holes, thus the effect of the substrate on the mechanical properties of the valves was eliminated. **Figure 7a** presents a sequence of images of transferring and mounting a deposited isolated valve from the substrate to a hole (see also Movie S4, Supporting Information). After mounting the valves on their predefined holes, deformation experiments were performed by FMT-120 in situ determine the required force for breaking the valves grown at 28 and 46 PSU. Also, SEM images were acquired throughout the deformation process (Movie S5, Supporting Information). As shown in **Figure 7b**, during the deformation, the fracture took place in the middle of the valve, and the crack propagated through the ribs and areole pores toward the periphery. The obtained mechanical strength of the valves revealed substantial differences for these two salinities. The required force for breaking valves at 28 PSU was  $12.53 \pm 1.43 \mu\text{N}$ . In contrast, valves grown at 46 PSU did not have the same mechanical strength and only  $5.10 \pm 2.04 \mu\text{N}$  was necessary to break them (**Figure 7c**). In order to understand how salinity level regulated the mechanical strength of valves, TEM image analysis was conducted to measure the thickness of the valves (**Figure S6**, Supporting Information). The mean thickness of the ribs and cross-connections of the whole valves decreased from  $54 \pm 6$  to  $19 \pm 8$  nm by increasing the salinity from 28 to 46 PSU.

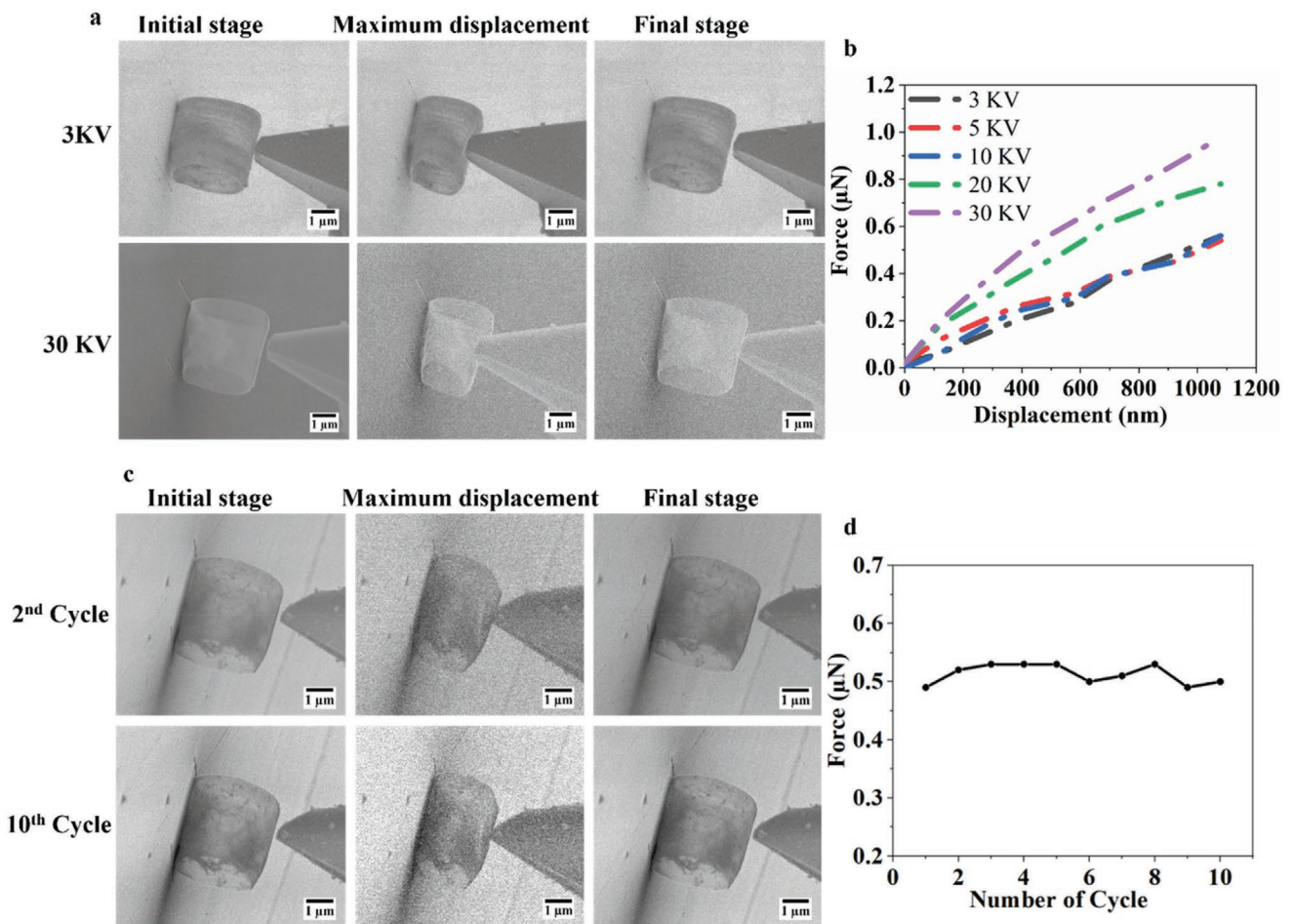


**Figure 6.** a) SEM images of different states of deformation experiments of girdle bands at different applied accelerating voltages; 3 KV; 30 KV; b) load-displacement curves of an individual set of girdle bands at different accelerating voltages. c) SEM images of different states of deformation experiments of girdle bands for different cycles; d) graph showing maximum force measurements in dependence of deformation cycle number of a set of girdle bands.

These findings suggest that a higher salinity level in the growth medium led to thinner valves, resulting in less mechanical strength, which is in agreement with the previous study revealing that ribs and cross-connections of the valves have a significant impact on the mechanical properties of frustule of *T.p.*<sup>[30]</sup> Determination of the Young's modulus of the biosilica in the valves is challenging due to their complex architecture. Potentially techniques like TEM electron tomography can provide a realistic model of complex morphologies at the micro and nano scale for FEM simulations,<sup>[58]</sup> however, a versatile workflow has not been developed for universal usage of ET data in FEM to date.

### 3. Conclusions

In summary, a workflow to characterize the mechanical properties of a biocomposite diatom frustule, on the micrometer scale has been developed. The workflow combines FIB micromachining, micromanipulators, and deformation tests with FEM simulations to determine the Young's modulus of biosilica. In

situ isolation, transfer, and deformation on different constituents, girdle bands and valves of diatom frustule, *T.p.*, were conducted inside a dual-beam SEM. The effects of salinity levels in the growth medium as well as electron beam damage on the mechanical properties of the frustule could be quantitatively established. The presented in situ sample preparation workflow preserves the delicate components of biocomposites and allows to quantify the mechanical properties of valves and girdle bands individually. Our approach can be extended to other species to accurately measure the mechanical properties of selected constituents of biocomposite materials at different hierarchical levels.

### 4. Experimental Section

**Diatom Culture:** *T.p.* (UTEX LB FD2) was obtained from the UTEX Culture Collection of Algae and incubated in artificial seawater supplemented with f/2 medium (ASW-f/2) at different salinity levels termed 28, 36, and 46 practical salinity unit (PSU). These are similar salinities, to which *T.p.* is known to be adaptive, the chemical effects on its frustule are well documented.<sup>[46]</sup> A climate cabinet (Flohr,

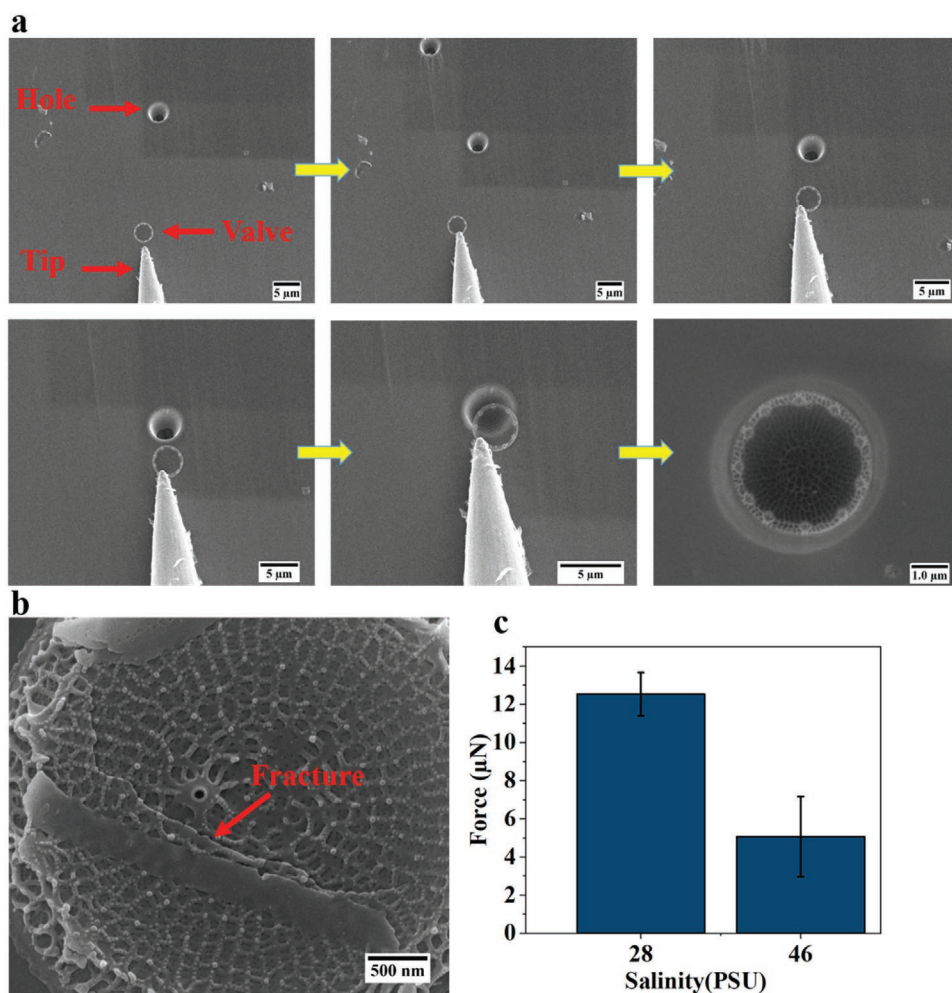


**Figure 7.** a) SEM images of the process of manipulation and transferring of an isolated valve of *T.p.* from the silicon wafer substrate to a prefabricated hole before the in situ deformation tests; b) SEM image of the fracture in a valve after deformation (the red arrow shows the fracture); c) bar graphs of required force for breaking the valves grown at salinities 28 and 46 PSU ( $n = 5$  valves per culture). Error bars indicate standard deviations.

Netherlands) with a light/dark cycle of 14 h/10 h at 23°C and a light intensity of 3000 Lux was employed to grow cell cultures. The cell cultures were shaken daily during the entire experiment to ensure appropriate mixing of the growth medium.

**Scanning Electron Microscopy Imaging and Energy-Dispersive X-Ray Spectroscopy (EDS) Elemental Mapping:** For SEM imaging of the intact frustule, a small amount of the critical point dried frustules (Section S1, Supporting Information) was deposited on a silicon wafer fixed to an SEM stub and sputter-coated with gold of less than 5 nm in thickness using a Quorum Q150T Plus-Turbo molecular pumped sputter coater. Before SEM imaging of the individual valve and girdle bands, the intact frustules were suspended in ethanol using a sonication bath (Bransonic ultrasonic cleaner, model 1510E-DTH, 42 kHz, USA) for 1 min to completely split girdle bands from the valves (although this method also often resulted in some broken valves and girdle bands). For EDS elemental mapping, intact frustules were deposited onto a standard aluminum SEM Stub. SEM imaging and EDS elemental mapping were conducted using dual-beam SEM Quanta 3D FEG (Thermo Fisher Scientific, USA), at an acceleration voltage of 5–10 kV. The applied electron dose during the deformation experiments were calculated using following equation

$$D = \frac{I \times t}{S} \quad (1)$$

where  $I$  is probe current,  $t$  is the imaging time, and  $S$  is the illuminated area.

**Focused Ion Beam-Scanning Electron Microscopy (FIB-SEM) and Micromanipulator:** In order to precisely separate valves and girdle bands from each other, the intact frustules of *T.p.* were deposited on a silicon wafer that was fixed to an aluminum SEM stub. The frustules laying on their girdle bands were selected for isolation of their valves from the girdle bands. The FIB milling process was carried out in a dual-beam SEM Quanta 3D FEG (Thermo Fisher Scientific, USA), equipped with a gallium ion ( $\text{Ga}^+$ ) source operating at an accelerating voltage of 30 kV. Because of the very delicate structure of the frustule of *T.p.*, employing a very low ion beam current (1.5 pA) during a single line scan milling process was critical to prevent structural collapse. Higher currents of the ion beam ( $I \geq 10$  pA) as well as multiple line scans with the current of 1.5 pA, notably damaged the girdle bands as well as valves and led to the structural collapse of the entire frustule. SEM images illustrating the effects of different milling parameters are shown in Figure S10 (Supporting Information). One of the crucial aspects of isolating the valves from the girdle bands of *T.p.* was to cut a line between valves and girdle bands, narrow and accurate enough not to cause any significant asymmetry to their overall topology. After cutting the valves from the girdle bands, a micromanipulator (MM3A-EM, Kleindiek Nanotechnik GmbH, Germany) was employed to separate them. The micromanipulator provided a high positional accuracy ( $\approx 10$  nm) for the

mechanical movement in three axes inside the SEM chamber. A sharp tungsten tip ( $\approx 150$  nm in radius) attached to the micromanipulator was employed for the manipulation of the valves. After complete isolation of the valve by the tip, the valve was transferred using the tip to another area of the substrate where a hole with a diameter in the range of a valve diameter had been prefabricated by FIB milling.

*In Situ Deformation Experiments:* Mechanical experiments on isolated girdle bands and valves were conducted using a force measurement unit (FMT-120) mounted on the MM3A-EM micromanipulator inside the FIB-SEM chamber. Throughout the deformation experiments, the force measurement system (FMS) provided force-time data which could be converted to force–displacement information via SEM image analysis. To do so, SEM micrographs were acquired continuously throughout the experiment. Then, the displacements were determined by following the positional change of the edge of the girdle bands. Correlated displacements of the girdle bands with various times were determined using a Gatan Digital Micrograph and, subsequently, the corresponding applied force on the girdle bands was noted for each displacement point. The deformation experiments on the girdle bands were carried out in a controlled displacement mode, where the tip was moved toward the girdle bands until the desired deformation was obtained. Furthermore, to monitor the influence of deformation rate on the mechanical properties of girdle bands, a series of experiments were conducted on a set of isolated girdle bands with different loading rates. As seen in Figure S11 (Supporting Information), lowering the rate of deformation resulted in a slight decrease in measured load. It should be noted that deformation cycle experiments were carried out in low vacuum mode SEM (LVSEM) at 10 kV with relative humidity of 4.3%. In addition, the necessary force for breaking the valves was measured via the deformation tests on the isolated valves mounted on prefabricated holes.

*Finite Element Simulations:* Finite element method simulations (FEM) are conducted using the FEM software package MSC.Marc. The mesh of the girdle bands consists of 24 900 linear hexahedral brick elements and its intrinsic mechanical response is modelled linear elastically. The geometry of the girdle bands over the length of the cylinder is simplified and assumed to have a uniform thickness over the complete length, where both overlap of the individual girdle bands and pores are not taken into account. The indenter itself is modeled as an impenetrable surface with an infinite stiffness. The bottom of the girdle bands is fixed to the substrate in the  $x$ - $y$ -plane where it is touching the surface of the sample holder. A load case is specified which describes the  $z$ -displacement of the indenter identical to the compression experiment as performed inside the SEM.

## Supporting Information

Supporting Information is available from the Wiley Online Library or from the author.

## Acknowledgements

The authors would like to thank Dr. Igor Zlotnikov at TU Dresden for his help at the initial stages of the project. The authors would also like to thank Mr. Siyamak Parsa for his practical assistance with the schematic illustration of the workflow. This research was carried out under project number C16030a in the framework of the Partnership Program of the Materials innovation institute M2i (www.m2i.nl) and the NWO Domain Science, which is part of the Netherlands Organization for Scientific Research (www.nwo.nl).

## Conflict of Interest

The authors declare no conflict of interest.

## Data Availability Statement

The data that support the findings of this study are available from the corresponding authors upon reasonable request.

## Keywords

biosilica, diatom frustule, hybrid materials, in situ deformation, micromanipulation

Received: June 13, 2021  
Revised: September 17, 2021  
Published online:

- [1] W. Al Zoubi, M. P. Kamil, S. Fatimah, N. Nisa, Y. G. Ko, *Prog. Mater. Sci.* **2020**, 112, 100663.
- [2] H. B. Yao, H. Y. Fang, Z. H. Tan, L. H. Wu, S. H. Yu, *Angew. Chem.* **2010**, 122, 2186.
- [3] R. F. Gibson, *Compos. Struct.* **2010**, 92, 2793.
- [4] A. Ali, A. Andriyana, *RSC Adv.* **2020**, 10, 16390.
- [5] Y.-Y. Kim, J. D. Carloni, B. Demarchi, D. Sparks, D. G. Reid, M. E. Kunitake, C. C. Tang, M. J. Duer, C. L. Freeman, B. Pokroy, *Nat. Mater.* **2016**, 15, 903.
- [6] A. Arakaki, K. Shimizu, M. Oda, T. Sakamoto, T. Nishimura, T. Kato, *Org. Biomol. Chem.* **2015**, 13, 974.
- [7] G. M. Luz, J. F. Mano, *Compos. Sci. Technol.* **2010**, 70, 1777.
- [8] B. Ji, H. Gao, *J. Mech. Phys. Solids* **2004**, 52, 1963.
- [9] F. Libonati, M. J. Buehler, *Adv. Eng. Mater.* **2017**, 19, 1600787.
- [10] A. Ghazlan, T. Ngo, P. Tan, Y. M. Xie, P. Tran, M. Donough, *Composites, Part B* **2020**, 205, 108513.
- [11] J. E. Rim, P. Zavattieri, A. Juster, H. D. Espinosa, *J. Mech. Behav. Biomed. Mater.* **2011**, 4, 190.
- [12] M. Grossman, D. Pivovarov, F. Bouville, C. Dransfeld, K. Masania, A. R. Studart, *Adv. Funct. Mater.* **2019**, 29, 1806800.
- [13] E. Munch, M. E. Launey, D. H. Alsem, E. Saiz, A. P. Tomsia, R. O. Ritchie, *Science* **2008**, 322, 1516.
- [14] H. D. Espinosa, J. E. Rim, F. Barthelat, M. J. Buehler, *Prog. Mater. Sci.* **2009**, 54, 1059.
- [15] B. Ji, H. Gao, *Annu. Rev. Mater. Res.* **2010**, 40, 77.
- [16] M. A. Meyers, P.-Y. Chen, A. Y.-M. Lin, Y. Seki, *Prog. Mater. Sci.* **2008**, 53, 1.
- [17] P.-Y. Chen, A. Lin, Y.-S. Lin, Y. Seki, A. Stokes, J. Peyras, E. Olevsky, M. A. Meyers, J. McKittrick, *J. Mech. Behav. Biomed. Mater.* **2008**, 1, 208.
- [18] J. Wang, Q. Cheng, Z. Tang, *Chem. Soc. Rev.* **2012**, 41, 1111.
- [19] M. Hildebrand, *Chem. Rev.* **2008**, 108, 4855.
- [20] Y. Wang, J. Cai, Y. Jiang, X. Jiang, D. Zhang, *Appl. Microbiol. Biotechnol.* **2013**, 97, 453.
- [21] M. Soleimani, L. Rutten, S. P. Maddala, H. Wu, E. D. Eren, B. Mezari, I. Schreur-Piet, H. Friedrich, R. A. van Benthem, *Sci. Rep.* **2020**, 10, 19498.
- [22] N. Kröger, N. Poulsen, *Annu. Rev. Genet.* **2008**, 42, 83.
- [23] Y. Wang, D. Zhang, J. Cai, J. Pan, M. Chen, A. Li, Y. Jiang, *Appl. Microbiol. Biotechnol.* **2012**, 95, 1165.
- [24] J. W. Goessling, Y. Su, C. Maibohm, M. Ellegaard, M. Kühl, *J. R. Soc. Interface Focus* **2019**, 9, 20180031.
- [25] E. Kumari, S. Görlich, N. Poulsen, N. Kröger, *Adv. Funct. Mater.* **2020**, 30, 2000442.
- [26] C. E. Hamm, R. Merkel, O. Springer, P. Jurkojc, C. Maier, K. Prechtel, V. Smetacek, *Nature* **2003**, 421, 841.
- [27] Z. H. Aitken, S. Luo, S. N. Reynolds, C. Thaulow, J. R. Greer, *Proc. Natl. Acad. Sci. USA* **2016**, 113, 2017.

- [28] N. Almqvist, Y. Delamo, B. Smith, N. Thomson, Å. Bartholdson, R. Lal, M. Brzezinski, P. Hansma, *J. Microsc.* **2001**, 202, 518.
- [29] D. Losic, K. Short, J. G. Mitchell, R. Lal, N. H. Voelcker, *Langmuir* **2007**, 23, 5014.
- [30] S. Görlich, D. Pawolski, I. Zlotnikov, N. Kröger, *Commun. Biol.* **2019**, 2, 245.
- [31] E. Topal, H. Rajendran, I. Zgłobicka, J. Gluch, Z. Liao, A. Clausner, K. J. Kurzydowski, E. Zschech, *Nanomaterials* **2020**, 10, 959.
- [32] J. Romann, M. S. Chauton, S. M. Hanetho, M. Vebner, M. Heldal, C. Thaulow, O. Vadstein, G. Tranell, M.-A. Einarsrud, *J. Porous Mater.* **2016**, 23, 905.
- [33] C. Jiang, H. Lu, H. Zhang, Y. Shen, Y. Lu, *Scanning* **2017**, 2017, 6215691.
- [34] M. S. Wang, I. Kaplan-Ashiri, X. L. Wei, R. Rosentsveig, H. D. Wagner, R. Tenne, L. M. Peng, *Nano Res.* **2008**, 1, 22.
- [35] Z. Shan, *Jom* **2012**, 64, 1229.
- [36] H. Asayesh-Ardakani, W. Yao, Y. Yuan, A. Nie, K. Amine, J. Lu, R. Shahbazian-Yassar, *Small Methods* **2017**, 1, 1700202.
- [37] C. Shi, D. K. Luu, Q. Yang, J. Liu, J. Chen, C. Ru, S. Xie, J. Luo, J. Ge, Y. Sun, *Microsyst. Nanoeng.* **2016**, 2, 16024.
- [38] X. Zhou, T. Li, Y. Cui, Y. Fu, Y. Liu, L. Zhu, *ACS Appl. Mater. Interfaces* **2019**, 11, 1733.
- [39] F. Komissarenko, G. Zograf, S. Makarov, M. Petrov, I. Mukhin, *Nanomaterials* **2020**, 10, 1306.
- [40] T. Przybilla, B. A. Zubiri, A. M. Beltrán, B. Butz, A. G. Machoke, A. Inayat, M. Distaso, W. Peukert, W. Schwieger, E. Spiecker, *Small Methods* **2018**, 2, 1700276.
- [41] P. A. Shade, M. A. Groeber, J. C. Schuren, M. D. Uchic, *Integr. Mater. Manuf. Innovation* **2013**, 2, 100.
- [42] N. Antoniou, K. Rykaczewski, M. D. Uchic, *MRS Bull.* **2014**, 39, 347.
- [43] J. Zang, L. Bao, R. A. Webb, X. Li, *Nano Lett.* **2011**, 11, 4885.
- [44] S. Romeis, J. Paul, P. Herre, D. de Ligny, J. Schmidt, W. Peukert, *Scr. Mater.* **2015**, 108, 84.
- [45] M. Yilmaz, N. Wollschläger, M. N. Esfahani, W. Österle, Y. Leblebici, B. E. Alaca, *Nanotechnology* **2017**, 28, 115302.
- [46] S. M. La Vars, M. R. Johnston, J. Hayles, J. R. Gascooke, M. H. Brown, S. C. Leterme, A. V. Ellis, *Anal. Bioanal. Chem.* **2013**, 405, 3359.
- [47] M. Sumper, E. Brunner, *ChemBioChem* **2008**, 9, 1187.
- [48] E. V. Armbrust, J. A. Berges, C. Bowler, B. R. Green, D. Martinez, N. H. Putnam, S. Zhou, A. E. Allen, K. E. Apt, M. Bechner, *Science* **2004**, 306, 79.
- [49] M. Johnston, J. Gascooke, A. Ellis, S. Leterme, *Analyst* **2018**, 143, 4930.
- [50] A. Bussard, E. Corre, C. Hubas, E. Duvernois-Berthet, G. Le Corguillé, L. Jourden, F. Couplier, P. Claquin, P. J. Lopez, *Environ. Microbiol.* **2017**, 19, 909.
- [51] H. Wu, H. Su, R. R. Joosten, A. D. Keizer, L. S. van Hazendonk, M. J. Wirix, J. P. Patterson, J. Laven, G. de With, H. Friedrich, *Small Methods* **2021**, 5, 2001287.
- [52] P. Schweizer, C. Dolle, D. Dasler, G. Abellán, F. Hauke, A. Hirsch, E. Spiecker, *Nat. Commun.* **2020**, 11, 1743.
- [53] A. I. Denisyuk, F. E. Komissarenko, I. S. Mukhin, *Microelectron. Eng.* **2014**, 121, 15.
- [54] A. I. Denisyuk, A. V. Krasavin, F. E. Komissarenko, I. S. Mukhin, *Adv. Imaging Electron Phys.* **2014**, 186, 101.
- [55] J. Paul, S. Romeis, J. Tomas, W. Peukert, *Adv. Powder Technol.* **2014**, 25, 136.
- [56] M. Mačković, F. Niekieł, L. Wondraczek, E. Spiecker, *Acta Mater.* **2014**, 79, 363.
- [57] Y.-J. Hu, G. Zhao, M. Zhang, B. Bin, T. Del Rose, Q. Zhao, Q. Zu, Y. Chen, X. Sun, M. de Jong, *Npj Comput. Mater.* **2020**, 6, 25.
- [58] P. Jimbert, M. Iturrondobeitia, R. Fernandez-Martinez, T. Guraya, J. Ibarretxe, *Adv. Mater. Res.* **2016**, 1139, 20.